



Surface Bragg gratings of proteins patterned on integrated waveguides for (bio)chemical analysis

Augusto Juste-Dolz¹ · Estrella Fernández¹ · Gloria Micó² · Luis A. Bru² · Pascual Muñoz² · Miquel Avella-Oliver^{1,3} · Daniel Pastor² · Ángel Maquieira^{1,3}

Received: 15 June 2023 / Accepted: 23 November 2023 / Published online: 29 December 2023
© The Author(s), under exclusive licence to Springer-Verlag GmbH Austria, part of Springer Nature 2023

Abstract

The incorporation of biomacromolecules onto silicon waveguiding microstructures constitutes a growing trend that pushes towards compact and miniaturized biosensing systems. This paper presents the integration of one-dimensional periodic nanostructures of proteins on the surface of micrometric silicon waveguides for transducing binding events between biomacromolecules. The study demonstrates this new bioanalytical principle by experimental results and theoretical calculations, and proves that rib waveguides (1–1.6- μm width) together with protein gratings (495–515-nm period) display suitable spectral responses for this optical biosensing system. Protein assemblies of bovine serum albumin are fabricated on the surface of silicon nitride waveguides, characterized by electron microscopy, and their response is measured by optical frequency domain reflectometry along the fabrication process and the subsequent stages of the biorecognition assays. Detection and quantification limits of 0.3 and 3.7 $\mu\text{g}\cdot\text{mL}^{-1}$, respectively, of specific antibodies are inferred from experimental dose–response curves. Among other interesting features, the results of this study point towards new miniaturized and integrated sensors for label-free bioanalysis.

Keywords Diffraction · Biosensor · Label-free · Immunoassay · Optical frequency domain reflectometry · Lab on a chip · Micrometric silicon waveguides

Introduction

Tailoring micro/nano-structured materials for biochemical analysis points towards the development of miniaturized and integrated biosensors capable of providing unique analytical solutions [1–7]. With the increasing demand for portable,

miniaturized, and integrated biosensors, the incorporation of biomacromolecules onto silicon-based waveguides has emerged as a paradigmatic approach [8–11]. These silicon-based waveguides are designed to guide electromagnetic waves through their core, with a part of the light interacting with biorecognition assays arranged on the surface of the guides. This strategy has witnessed significant scientific activity in recent years, with several flagship examples such as ring resonators, Mach–Zehnder interferometers, and Young interferometers [12–14].

A key challenge in this field relies on discovering and implementing new light-matter interaction phenomena that enable to transform recognition events between biomolecules into measurable signals. The impact of these findings is nowadays greatly supported by the advances on active and passive waveguiding materials, together with their combination to conceive integrated optical devices. This aspect paves the way for prospective biosensors that incorporate all the sensing elements (light sources, waveguides, detectors, etc.) in a monolithic chip [15–19].

✉ Miquel Avella-Oliver
miavol@upv.es

✉ Daniel Pastor
dpastor@dcom.upv.es

✉ Ángel Maquieira
amaquieira@qim.upv.es

¹ Instituto Interuniversitario de Investigación de Reconocimiento Molecular y Desarrollo Tecnológico (IDM), Universitat Politècnica de València, Universitat de València, 46022 Valencia, Spain

² Photonics Research Labs, ITEAM, Universitat Politècnica de València, 46022 Valencia, Spain

³ Departamento de Química, Universitat Politècnica de València, 46022 Valencia, Spain

In this study, the focus is placed on the implementation of one-dimensional periodic assemblies of proteins on the surface of micrometric silicon waveguides for transducing immunoassays (Fig. 1). This biosensing approach relies on gratings of biomolecules tailored to diffract incident light beams. When samples are incubated on these gratings, the patterned biomolecules bind their target molecules present in the sample, which increases the amount of matter that conforms the grating and the intensity of the diffracted signal becomes greater. As a result, the concentration of the target compound can be quantified in label-free conditions by means of the intensity of the diffracted signal. These biomolecular gratings can be patterned on solid substrates and irradiated with laser beams, thus using the intensity of the diffracted beams as analytical signal. This free-space diffractive strategy is a powerful label-free technique for biosensing, compatible with simple instrumentation, which has been successfully implemented for the detection of antibodies [20], proteins [21], and low-molecular weight organic compounds [22] among other targets.

One step beyond in these biosensors rely on patterning the biomolecular gratings on the surface of waveguiding materials, where the diffractive event takes place between the grating and the guided light. This approximation has been performed on slabs of tantalum pentoxide as waveguides with biomolecular gratings on their surface, which couple out part of the guided light as a response of the biomolecular assay. Among other strengths, this approach has been materialized in benchtop devices with great multiplexing possibilities [23, 24]. These diffractive gratings biomolecules

have also been implemented on optical fibers to transduce biorecognition events, being in this case both the incident light and the diffracted response propagated within the fiber [25]. Compared with other bioanalytical developments based on fiber Bragg gratings in the state-of-the-art [26–28], the Bragg grating in this new approximation is not etched in the core of the fiber, but it is constituted by the bioreceptors themselves patterned on the fiber. After preliminary insights into tapered optical fibers [25], the present study introduces these biomolecular Bragg gratings (BBGs) on photonic circuits (Fig. 1). An appealing feature of biosensing systems based on these diffractive gratings of biomolecules over other label-free methods relies on their capability to avoid signal contributions from non-specific binding [29]. This is an important advantage that point towards the direct analysis of unprocessed biological samples, as demonstrated in previous investigations [23, 25, 30]. The first implementation of this biosensing principle on photonic integrated circuits is herein reported, which provide insights into additional benefits of this diffractive biosensors in terms of integration and miniaturization.

This paper investigates these new optical materials for biosensing through both experimental results and theoretical calculations, examines the role of the main variables involved, and addresses the fabrication and characterization of the patterned bilayers. The paper also offers a perspective on the possibilities of Optical Frequency Domain Reflectometry (OFDR) for biosensing, and illustrates the bioanalytical potential of the approach through a model immunoassay to quantify antibodies in a label-free conditions.

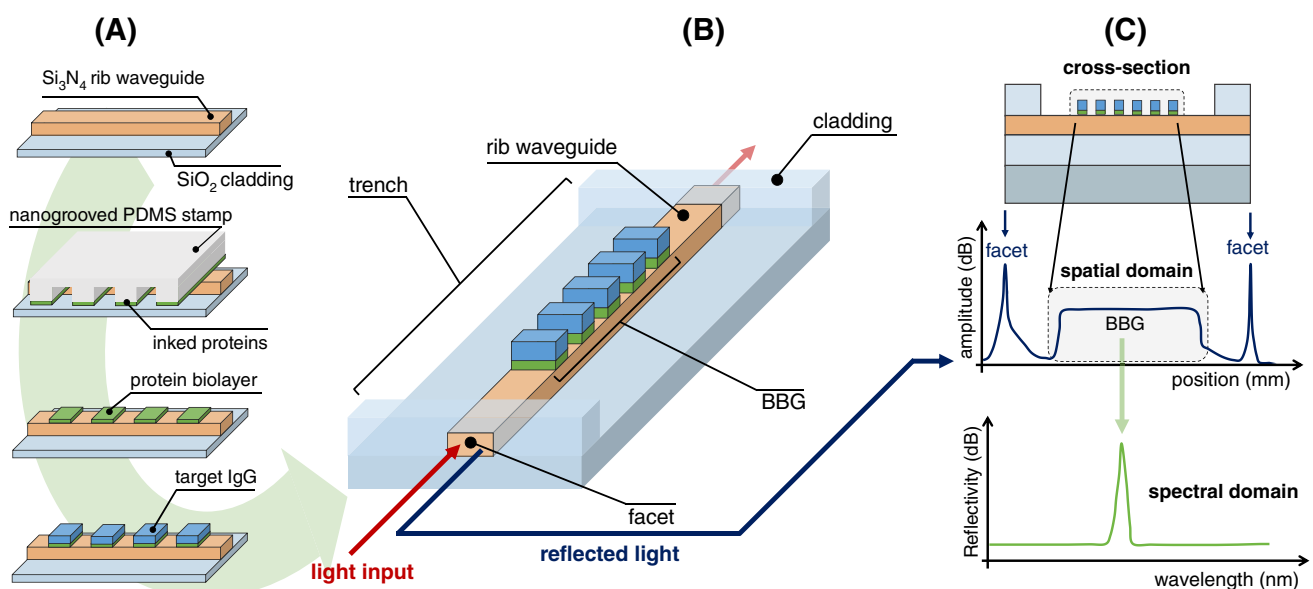


Fig. 1 General scheme of this biosensing principle based on periodic nanostructures of bioreceptors (BBGs) patterned on the surface of integrated waveguides. **(A)** Fabrication of protein gratings by micro-

contact printing on the waveguides, **(B)** photonic sensing device, and **(C)** the resulting optical signals

Experimental section

Electromagnetic simulations

Electromagnetic simulations to calculate the optical response of the system were carried out by means of finite difference method in the Quasi TE & TM approach, implemented on Matlab™ [31, 32]. The electromagnetic field distribution results were validated with commercial software MODE Lumerical (Finite Difference Eigenmode). The overlapping integrals (i.e. proportion of the total field interacting with the Bragg perturbation) were calculated from the obtained field distribution over the complete waveguide and compared with the field localized onto the BBG area. The conditions and the parameters of the waveguides that were employed for the simulations are represented in Figure S1. A refractive index of 1.43 was considered for the protein bilayers [33].

Waveguide fabrication

The fabrication process starts by growing a 2.5- μm -thick SiO_2 buffer by thermal oxidation of a Si wafer of 100 mm (4 in). Following, a 300-nm layer of Si_3N_4 is deposited by low-pressure chemical vapour deposition. In the next step, the waveguide cross-sections are patterned by photo-lithography employing an i-line stepper, whose minimum feature size is 500 nm. Afterwards, the definition of the core cross section is accomplished by reactive ion etching of the silicon nitride film. Lastly, a SiO_2 cladding of 2- μm thickness is deposited by means of plasma enhanced chemical vapour deposition, whereby the guides are fully defined. After the waveguide fabrication steps, air wells (trenches) are created by selectively etching away the cladding oxide, where the waveguide core becomes in direct contact with the surrounding media (Figure S2) [34].

Fabrication of the BBGs

Nanogrooved microcontact printing stamps were created by dispensing a mixture of polydimethylsiloxane (PDMS) monomer and curing agent (10:1 w/w) onto the structured side of a silicon master (period 416 nm, 100-nm groove depth, and duty cycle 50%). Next, the mixture was degassed in a vacuum chamber for 30 min, and cured overnight at 60°C. Thereafter, the polymerized PDMS was peeled off from the master and chopped into squared pieces (2 \times 2 mm). The resulting stamps were sonicated three times for 5 min in ethanol (30% in MilliQ water) and air dried before use (see Figure S3 for a FESEM characterization of the stamp surface). Then, a solution of 250 $\mu\text{g}\cdot\text{mL}^{-1}$ of bovine serum albumin (BSA) in sodium phosphate buffer (8 mM Na_2HPO_4 , 2 mM KH_2PO_4 , 137 mM NaCl, 2.7 mM KCl, milliQ water, pH 7.4) was incubated onto the structured side

of the stamps for 160 min at room temperature. Next, the stamps were cleaned with milliQ water and air dried. Then, the structured side of the stamp was placed in contact with the silicon photonic platform for 20 min to transfer the BSA proteins to the top surface of the waveguides. This stamping step was performed using a custom mechanical setup to apply a controlled and reproducible stamping pressure (Figure S4) to overcome the trench and reach the waveguide surface (Figure S5). Finally, the stamps were removed and the waveguides with the patterned BBGs were rinsed with PBST (sodium phosphate buffer with polysorbate 20 at 0.05% v/v) and water, and air dried.

Characterization of the BBGs

The structural characterization of the BBGs was performed by Field Emission Scanning Electron Microscopy (FESEM, ZEISS ULTRA-55 microscope, ZEISS, Oxford Instruments). The period of the structures was calculated as the sum of the average width of the protein strips and the average width of the gaps between them, measured from the FESEM images. The duty cycle was calculated as the average width of the protein strips divided by the period and multiplied by 100.

Optical frequency domain reflectometry

For the optical measurements of the BBGs, light from a tunable infrared laser (1500–1600 nm) was coupled into the waveguides through the facets using lensed optical fiber pigtailed, and the reflected signal was acquired with an optical spectrum analyzer. The optical response in both space and spectral domains was acquired and analyzed by Optical Frequency Domain Reflectometry (OFDR) [35]. As

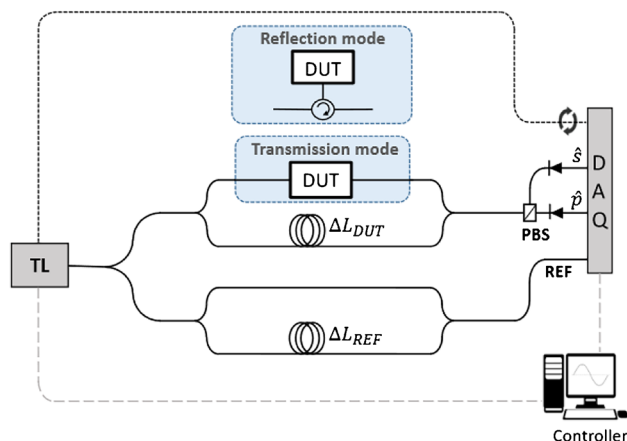


Fig. 2 Scheme of the optical setup employed to perform the OFDR measurements. TL: tunable laser, DUT: device under test (Si_3N_4 chip), PBS: polarization beam splitter, DAQ: digital acquisition card

illustrated in Figure S6, the setup for OFDR measurements is composed of two imbalanced Mach–Zehnder interferometers (MZI) in standard single-mode fibre, connected in parallel and fed by a scanning tunable laser (10 mW along 1490–1650 nm, Yenista TUNICs T100R). The lower MZI in Fig. 2 is employed as triggering, since the response of the upper MZI is resampled (offline) by points provided by the triggering MZI interferogram. This ensures that the response of the upper MZI is self-referenced against possible nonlinearities of the continuous scan of the tunable laser. Finally, the signals are collected by a digital acquisition card (National Instruments USB-6259).

Time/distance event information is a key OFDR feature since it allows to eliminate spurious reflections in the facets and unwanted transitions along the photonic path, and most importantly, to focus onto the BBG interaction range as indicated in Fig. 1. The time/distance events of the protein patterns (amplitude and phase) are isolated by applying the inverse fast Fourier transform to the interferogram. Once isolated, the BBG regions of the OFDR spectra were converted to the spectral domain in the logarithmic scale. The equivalence between logarithmic and linear scale was $\text{dB} = 10 \cdot \log_{10} \left(\frac{P_1}{P_0} \right)$, where dB is the value of the power in logarithmic scale, P_1 is the intensity level in linear scale, and P_0 is the reference power level of the employed optical instrumentation. Then, the reflection peaks in the linear scale were integrated to provide the overall reflectivity of the BBG.

Immunoassays

To perform the biorecognition assays, solutions of antiBSA specific IgG ($0\text{--}100 \mu\text{g}\cdot\text{mL}^{-1}$) in PBST were incubated onto the BBGs. After 20 min of incubation, the photonic platforms were rinsed with PBST and milliQ water and air dried. A scheme of the overall process is illustrated in Fig. 1 A.

To quantify the experimental sensitivity, ten replicates of blank samples ($0 \mu\text{g}\cdot\text{mL}^{-1}$ of IgG) were measured to calculate the mean value (M_{blank}) and the standard deviation (SD_{blank}) of this set of ten reflectivity signals. The limit of detection was considered as the concentration obtained by interpolating the signal value of $M_{\text{blank}} + 3 \cdot SD_{\text{blank}}$ in the sigmoidal fitting of the dose–response curve. The same approach was used to determine the limit of quantification but interpolating $M_{\text{blank}} + 10 \cdot SD_{\text{blank}}$ in this case.

Regeneration

To regenerate the waveguides after performing immunoassays on patterned BBGs of proteins, the silicon chips were sonicated for 10 min in a mixture of H_2O_2 (30%)/ NH_4OH (32%)/ H_2O (1:1:2). The process was repeated three times, and then the chips were rinsed with milliQ water. Finally,

substrates were sonicated for 5 min in milliQ water, and dried under a stream of air. A FESEM image of a waveguide with a patterned BBG and its reflection spectra before and after performing the regeneration are shown in Figure S6. The experiments reported in this paper were performed with chips regenerated up to 10 times, where chips with different regeneration cycles were used indistinctly along study, obtaining the consistent results discussed above.

Results and discussion

Detection principle

The detection principle behind this approach relies on periodic nanostructures of bioreceptors patterned on the surface of integrated waveguides. These nanostructures are constituted by periodic strips of proteins and empty gaps between them, and the periods of these patterns are tailored to act as Bragg gratings that interact with the evanescent field of the light propagated through the waveguide. As schematized in Fig. 1, this diffractive light–matter interaction reflects part of the guided light, which remains guided and displays a peak in the reflection spectrum. When samples are incubated on the photonic chips, the patterned protein probes bind their target molecules present in the sample, which increases the periodic refractive index modulation that conforms the grating and the reflected light becomes enhanced. As a result, the concentration of target molecules in solution can be quantified, in label-free conditions, through the intensity of the reflected peak.

To experimentally measure the response of the immunoassays taking place in the biomolecular gratings, the optical signals were collected and processed by Optical Frequency Domain Reflectometry (OFDR) [35, 36]. OFDR is a powerful interrogation technique for sensing [36], which relies on an interferometric setup that allows to determine the longitudinal position at which each reflective event takes place within the waveguide (Figure S6). Nonetheless, OFDR remains unexplored for biosensing. To the best of our knowledge, only one recent study reports its use in biosensing [37], and OFDR has never been combined with Bragg gratings for bioanalytical purposes as herein.

Combining OFDR and protein gratings provides simultaneous information on both the position of the protein gratings distributed along the waveguide as well as their spectral response (Fig. 1C). Using both parameters together enable a fine selection of the analytical signal and a rich characterization of the system. On the one hand, for the measurements in this work, light from a tunable infrared laser (1500–1600 nm) was coupled into the waveguides through their facets (Fig. 1B), and the reflection generated by the in and out facets is much more intense

than that for the protein gratings. Using OFDR together with the protein gratings conveniently allows to identify the diffracted peak of the patterned biorecognition assays and to discriminate it from the background signal coming from the facets (Fig. 1C). On the other hand, this OFDR implementation introduces appealing multiplexing perspectives for biosensing in distributed waveguides [36].

Theoretical calculations

The light-matter interaction phenomena projected in this investigation requires a suitable contribution of light

propagating through the top surface of the guide, on which the patterned protein bilayers are placed. Photonic circuits constituted by rib waveguides of silicon nitride with a fixed thickness of 300 nm and widths from 1.0 to 1.6 μm are herein assessed, and the results (Fig. 3A and Figure S1) indicate that an important part of the fundamental mode propagates through the top surface of these planar waveguides. As observed in Fig. 3 B, the magnitude of this evanescent field decreases with the waveguide width and slightly increases with the wavelength, reaching about 13.5% of the total field intensity of the guided mode for 1 μm waveguides at $\lambda = 1550 \text{ nm}$, which supports the capability of

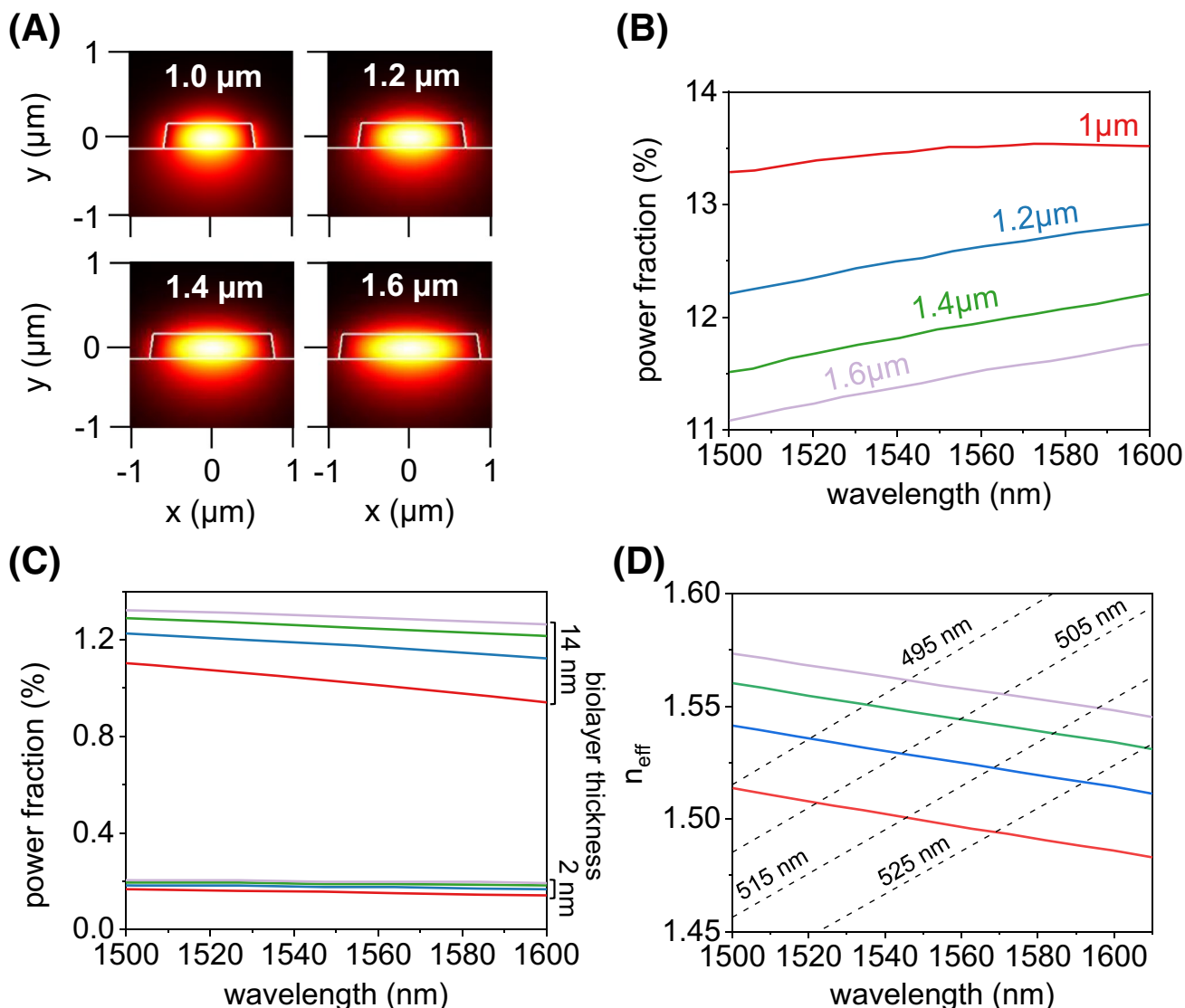


Fig. 3 Results of the theoretical calculations. **A** Spatial distribution of the field intensity (fundamental mode, $\lambda = 1550 \text{ nm}$) for different waveguide widths. **B** Fraction of light power of the evanescent field in the external medium (air) for different waveguide widths and input wavelengths. **C** Fraction of light power in the evanescent field within two different thicknesses of protein layers on the top surface of the

guide, for different waveguide widths (color code in **B**) and wavelengths. **D** Effective refractive indexes for a range of guided wavelengths and waveguide widths (solid lines, color code in **B**), together with the Bragg equation at each condition (dashed lines)

these waveguides to sense interactions within the evanescent field.

The power fraction of the guided mode for protein biolayers was also calculated for different waveguide widths. As shown in Fig. 3 C, the intensity of the evanescent field contained within different biolayer thicknesses on the top of the waveguide increases together with this thickness. This calculation includes a common value for a protein monolayer (2 nm) and a typical thickness after a subsequent binding of specific antibodies (14 nm), and the result suggests a suitable distribution of energy to sense changes in the biolayer thicknesses induced by biorecognition events. It can also be observed that the power fraction slightly increases together with the waveguide width. The guided mode is less confined and expands vertically (Fig. 3B) when this width decreases, which distributes the transverse profile of the guided mode in a broader area, and the amount of available energy in a thin layer becomes reduced.

The width of the waveguides also determines the grating periods that meet the Bragg condition and the spectral response of the patterned biolayers. Figure 3 D shows the simulated values of the effective refractive index as a function of the guided wavelength and the waveguide width (solid lines). The Bragg condition is satisfied by $\lambda_B = 2n_{eff} \cdot \Lambda$, where n_{eff} is the effective refractive index and Λ is the Bragg period. Note that n_{eff} also depends on the wavelength and the Bragg condition is expressed as $\lambda_B/2\Lambda = n_{eff,\lambda_B}$. In the figure, the left side of the equation is represented for different Bragg periods (dashed lines), and the crossing points between the two sets of curves indicate the corresponding λ_B values. As shown in Fig. 3 D, within the expected range of effective refractive index for these structures surrounded by air [38], grating periods from 495 to 525 nm display an appropriate response for the spectral window of the standard near-infrared analyzers typically employed for these waveguides.

Fabrication and characterization

The optical waveguides for this investigation were fabricated by standard photolithographic procedures. A silica cladding is included at the edges of the chip to meet the light coupling conditions, and the top surface of the guides is uncovered for patterning the protein BBGs on them and for the subsequent incubation of samples (Figures S2 and S5).

In this study, the BBGs were patterned on the guides by microcontact printing. This is a versatile technique based on creating stamps of polydimethylsiloxane by replica molding from a master structure, inking biomacromolecules on the stamps, and then transferring them onto solid surfaces by stamping (Fig. 1A) [22, 39, 40]. As shown in Fig. 4 A, this approach provides periodic protein nanostructures onto the top surface of the waveguides, defined

by a period of 415.6 ± 2.4 nm and a duty cycle of $48 \pm 5\%$. This characterization also suggests an accumulation of biological matter onto the strips of the protein nanostructures after incubating specific IgG targets (Fig. 4A iii), which indicates that the patterning process keeps the functionality of the binding sites of the patterned proteins. It is also worth mentioning that the flexibility of the polydimethylsiloxane allows it to overcome the height of the cladding and to reach the top surface of the waveguide for a suitable protein transfer (Figure S5), which means an interesting new insight into the versatility of microcontact printing to pattern biomolecules.

As commented above, the optical response of the biosensor depends on the period of the BBG, and this parameter was adjusted by controlling the angle between the grooved relief of the stamp and the longitudinal direction of the guide in the stamping stage (Figures S4, S5, S7, and Table S1). Patterning different periods by microcontact printing enables tuning the wavelength of the reflection peak without requiring additional master structures. As observed in Fig. 4 B (see also Figures S8–S11), the resulting period scales exponentially with the stamping angle. Stamping angles between 32° and 38.6° yield protein grating periods whose reflection peak falls within the spectral window selected from the theoretical calculations (490–530 nm, Fig. 3C) for these waveguides (Table S1).

Optical response

To prove the concept, the optical response of the protein nanostructures was measured at each step of the BBG fabrication and after incubating a selective antibody [30], using a representative model immunoassay based on BSA probes and antiBSA IgGs as targets. These results are presented in Fig. 5A, where the higher reflection peaks observed at 0 and 5 mm correspond to the facets and the less intense peaks at 1 and 4 mm correspond to the cladding transitions of the trench. As expected for the raw waveguides without protein gratings, no signals are observed between the two peaks of the cladding transitions (BBG region) neither in the spatial domain nor in the spectral domain data. After stamping the protein BBGs, the amplitude signal increases in the central part of the spatial domain data (BBG region, see also Figure S12) and a reflection peak appears in the spectral domain at 1578 nm. This reflection peak meets the Bragg condition for a BBG period of 525 nm and corroborates the patterned transfer of proteins to the waveguide surface (Table S1). Finally, the incubation of specific IgG ($100 \mu\text{g}\cdot\text{mL}^{-1}$) displays an enhancement of about one order of magnitude in the reflection peak of the spectral domain, which is not observed after incubating only buffer solution (Figure S13). Together with the previous FESEM

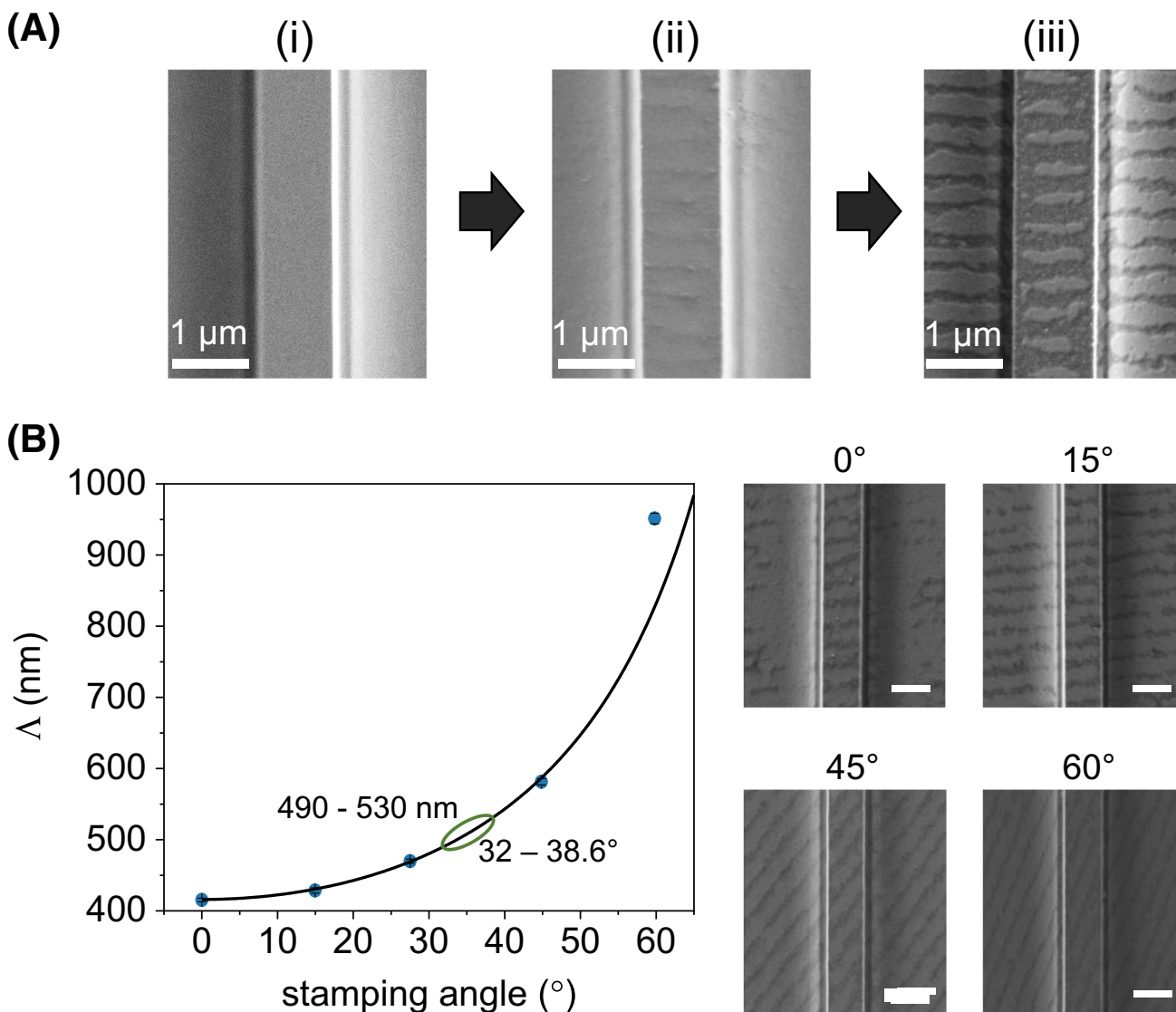


Fig. 4 **A** FESEM images of a 1- μm waveguide (i) before and (ii) after patterning a BBS of BSA by microcontact printing, and (iii) after the incubation of specific antiBSA IgGs ($10 \mu\text{g}\cdot\text{mL}^{-1}$). **B** Experi-

mental (blue dots) and simulated (black line) periods of the protein nanostructures for different patterning angles, and the corresponding FESEM images of the protein BBSs (scale bars: $1 \mu\text{m}$)

characterization, these results indicate that the biomolecular gratings are functional and demonstrate the initial hypothesis of this new photonic principle for biosensing.

Then, it was explored and compared the experimental response of the BBSs on waveguides of different widths. As observed in Fig. 5 B, the position of this reflection peak shifts to higher wavelengths with increasing waveguide widths, and this trend follows the cosine response predicted by the simulations. The experimental BBS peaks for 1.4- and 1.6- μm waveguides fall outside the measuring window of the employed OFDR analyzer (1525–1610 nm), and the reflection peak for 1- and 1.2- μm waveguide widths appear within this range. In particular, the BBS peak of the protein gratings in $1 \mu\text{m}$ waveguides

is centred in the measuring window (1568 nm), and these waveguides were selected for the subsequent experimental assessment of the label-free biosensing capabilities of this approach (Table S1).

Immunosensing and analytical features

BBSs of BSA probes were patterned on a set of chips and incubated with increasing concentrations of specific antiBSA IgG targets in buffer to perform an experimental dose–response curve. The difference in the area of the reflection peak before and after incubating specific targets was employed as the analytical signal, since it represents the

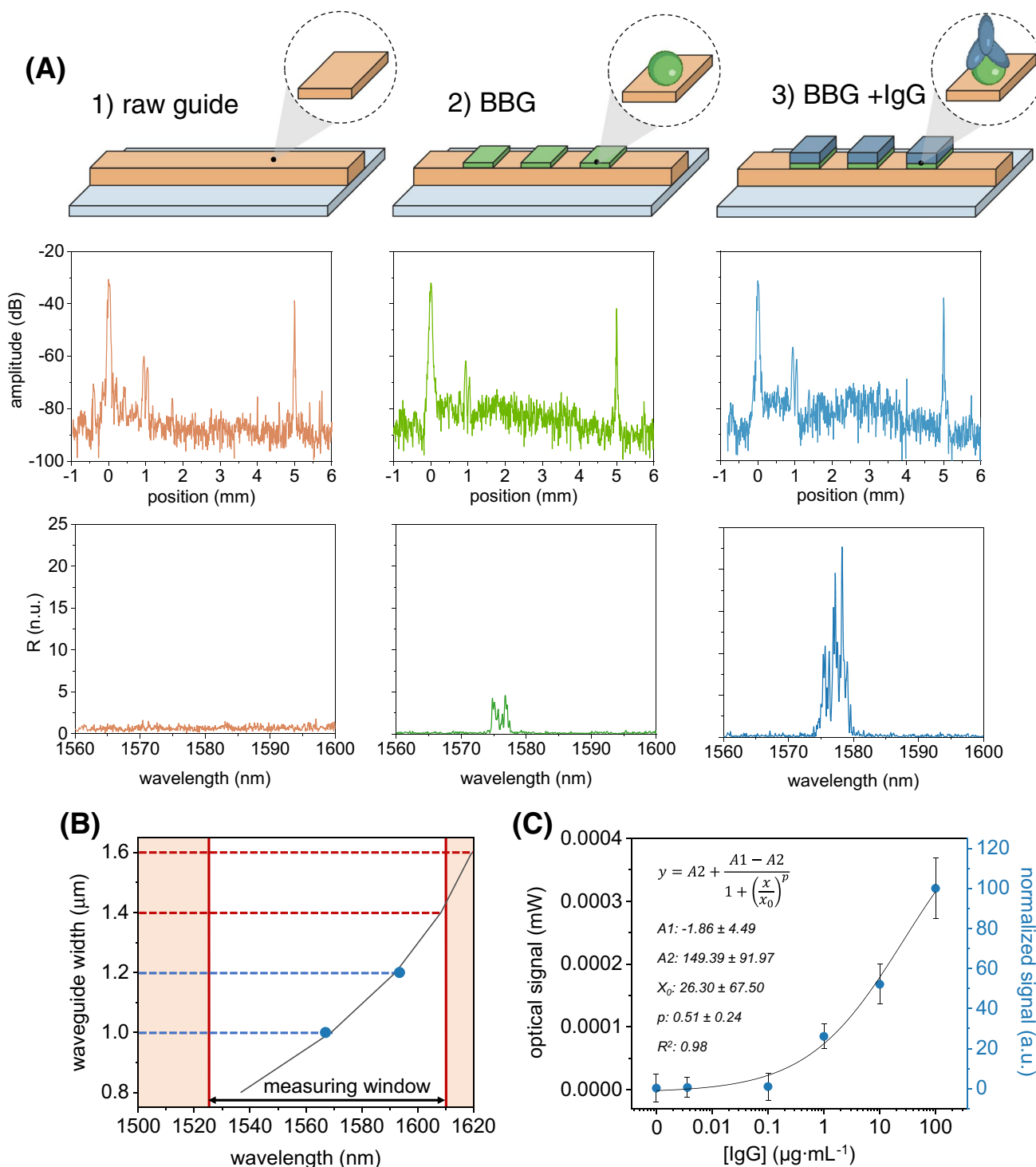


Fig. 5 **A** Reflection spectra processed by OFDR in the (i) spatial and (ii) spectral domains. The optical measurements were performed before and after patterning BBGs of BSA proteins onto a $1 \mu\text{m}$ waveguide and after incubating a solution of specific antiBSA IgG targets ($100 \mu\text{g}\cdot\text{mL}^{-1}$). **B** Position of the reflected peak for each waveguide width. The black line represents the simulated trend, and the blue dots show the experimental results obtained with protein BBGs (period of

525 nm) patterned on waveguides of different widths. **C** Experimental dose–response immunoassay curve fitted to a sigmoidal (logistic 4-parameter) regression. The experimental parameters of the sigmoidal fitting are indicated within the graph. Three replicate measurements were performed for each concentration. The right axis indicates the signal normalized in percentage, using the reflectivity the reflectivity obtained after the incubation of $100 \mu\text{g}/\text{mL}$ of IgG as reference

overall change of the reflected power. As shown in Fig. 5 C, the enhancement of the peak reflectivity is proportional to the concentration of targets and correlates well with a 4-parameter logistic curve. Relative standard deviations in the reflectivity signal within the 15–20% range are displayed by the higher IgG concentrations measured in this experiment. From this dose–response curve, an experimental detection limit of $0.3 \mu\text{g}\cdot\text{mL}^{-1}$ and quantification limit of $3.7 \mu\text{g}\cdot\text{mL}^{-1}$ of specific IgG were inferred. Those are promising values, especially considering that it is a label-free system and that this is the first demonstration of this transduction mechanism in integrated waveguides. Another interesting aspect to highlight is the possibility to regenerate the waveguides for performing further experiments on them (Figure S6). This regeneration is a valuable advantage to simplify and minimize the costs and ecological fingerprint of prospective research and development activities for BBG-based systems as well as for other photonic biosensors.

Future perspectives

The outcome of this investigation suggests future innovations for the monolithic integration of active components (light sources, detectors, etc.) in silicon-based waveguides with BBGs, to conceive fully integrated photonic devices for point-of-care biosensing [41]. Along these lines, other advances on patterning bilayers on surfaces may be compatible with this BBG concept and support its scope [20, 30, 42]. Also, the easy tunability of the BBG peak as well as the OFDR interrogation introduces great possibilities to perform and quantify multiple assays in a single analysis [25]. Regarding OFDR, this feature comes from the capability of this interrogation technique to easily discriminate and quantify reflective signals generated at different positions along a single waveguide. Therefore, this capability introduces appealing multiplexing perspectives by distributing many assays in each waveguide of a photonic chip containing hundreds of waveguides. Besides, transducing biorecognition events using diffractive biological gratings entails a unique potential to avoid signal contributions from non-specific bindings [23, 30]. In general, all these advantages together point towards label-free biosensors, capable of performing and measuring many assays in a single integrated and miniaturized chip, and solving non-specific binding issues in the direct analysis of untreated biological samples.

Conclusions

This study showcases this novel diffractive biosensing principle on photonic integrated waveguiding platforms. It also confirms the capability of microcontact printing

to create patterns of biomacromolecules onto rib waveguides, preserving their binding functionality, overcoming the height step introduced by the cladding trench, and tuning the optical response of the biosensor by just controlling the stamping angle. The experimental results with a model immunoassay demonstrates that the intensity of the reflection peak from protein gratings after interacting with specific IgGs follows the characteristic dose–response behavior for quantitative biosensing systems. This study charts a promising path for the advancement of these diffractive biosensors and points towards miniaturized photonic devices for the direct analysis of samples.

Supplementary Information The online version contains supplementary material available at <https://doi.org/10.1007/s00604-023-06124-z>.

Acknowledgements The authors acknowledge Instituto de Microelectrónica de Barcelona CNM-CSIC for the support in the fabrication of the measured chip samples on the multiproject CNM-VLC silicon nitride technology platform.

Funding Funding was provided by grants PID2019-110713RB-I00, TED2021-132584B-C21, and PID2019-110877GB-I00 funded by MCIN/AEI/<https://doi.org/10.13039/501100011033> and co-funded by “ERDF A way of making Europe”, Ministerio de Economía y Competitividad (TEC2016-80385-P), Generalitat Valenciana (PROMETEO/2020/094, PROMETEO/2021/015, IDIFEDER/2021/046), and Universitat Politècnica de València (PAID-06–22).

Data availability The authors confirm that the data supporting the findings of this study are available within the article [and/or] its supplementary materials.

Declarations

Competing interests The authors declare no competing interests.

References

1. Khan SA, Khan NZ, Xie Y et al (2022) Optical sensing by metamaterials and metasurfaces: from physics to biomolecule detection. *Adv Opt Mater* 10:2200500. <https://doi.org/10.1002/adom.202200500>
2. Alba-Patiño A, Vaquer A, Barón E et al (2022) Micro- and nanosensors for detecting blood pathogens and biomarkers at different points of sepsis care. *Microchim Acta* 189:74. <https://doi.org/10.1007/s00604-022-05171-2>
3. Wang J, Maier SA, Tittel A (2022) Trends in nanophotonics-enabled optofluidic biosensors. *Adv Opt Mater* 10:2102366. <https://doi.org/10.1002/adom.202102366>
4. Amirjani A, Rahbarimehr E (2021) Recent advances in functionalization of plasmonic nanostructures for optical sensing. *Microchim Acta* 188:57. <https://doi.org/10.1007/s00604-021-04714-3>
5. Krämer J, Kang R, Grimm LM et al (2022) Molecular probes, chemosensors, and nanosensors for optical detection of biorelevant molecules and ions in aqueous media and biofluids. *Chem Rev* 122:3459–3636. <https://doi.org/10.1021/acs.chemrev.1c00746>

6. Yang T, Duncan TV (2021) Challenges and potential solutions for nanosensors intended for use with foods. *Nat Nanotechnol* 16:251–265. <https://doi.org/10.1038/s41565-021-00867-7>
7. Liu C, Huang J, Xu T, Zhang X (2022) Powering bioanalytical applications in biomedicine with light-responsive Janus micro-/nanomotors. *Microchim Acta* 189:116. <https://doi.org/10.1007/s00604-022-05229-1>
8. Luan E, Shoman H, Ratner D et al (2018) Silicon photonic biosensors using label-free detection. *Sensors* 18:3519. <https://doi.org/10.3390/s18103519>
9. Xu W, Liu J, Song D et al (2021) Rapid, label-free, and sensitive point-of-care testing of anti-SARS-CoV-2 IgM/IgG using all-fiber Fresnel reflection microfluidic biosensor. *Microchim Acta* 188:261. <https://doi.org/10.1007/s00604-021-04911-0>
10. Gupta R, Goddard NJ (2020) Leaky waveguides (LWs) for chemical and biological sensing—a review and future perspective. *Sensors Actuators B Chem* 322:128628. <https://doi.org/10.1016/j.snb.2020.128628>
11. Ettabib MA, Marti A, Liu Z et al (2021) Waveguide enhanced raman spectroscopy for biosensing: a review. *ACS Sensors* 6:2025–2045. <https://doi.org/10.1021/acssensors.1c00366>
12. Steglich P, Hülsemann M, Dietzel B, Mai A (2019) Optical biosensors based on silicon-on-insulator ring resonators: a review. *Molecules* 24:519. <https://doi.org/10.3390/molecules24030519>
13. Soler M, Estevez MC, Cardenosa-Rubio M et al (2020) How nanophotonic label-free biosensors can contribute to rapid and massive diagnostics of respiratory virus infections: COVID-19 case. *ACS Sensors* 5:2663–2678. <https://doi.org/10.1021/acssensors.0c01180>
14. Pawar D, Kale SN (2019) A review on nanomaterial-modified optical fiber sensors for gases, vapors and ions. *Microchim Acta* 186:253. <https://doi.org/10.1007/s00604-019-3351-7>
15. Artundo I (2017) Photonic Integration: new applications are visible. *Opt Photonik* 12:22–25. <https://doi.org/10.1002/opph.201700015>
16. Chen Z, Shi Y, Wei M, et al (2023) A universal approach to high-index-contrast flexible integrated photonics. *Adv Opt Mater* 11. <https://doi.org/10.1002/adom.202202824>
17. Chandrasekar R, Lapin ZJ, Nichols AS et al (2019) Photonic integrated circuits for Department of Defense-relevant chemical and biological sensing applications: state-of-the-art and future outlooks. *Opt Eng* 58:1. <https://doi.org/10.1117/1.OE.58.2.020901>
18. Ma Y, Zong Y, Yin H et al (2021) 2D Optical Waveguides based on hierarchical organic semiconductor single crystals. *Adv Opt Mater* 9:2101481. <https://doi.org/10.1002/adom.202101481>
19. Nikolaidou K, Condelipes PGM, Caneira CRF et al (2022) Monolithically integrated optical interference and absorption filters on thin film amorphous silicon photosensors for biological detection. *Sensors Actuators B Chem* 356:131330. <https://doi.org/10.1016/j.snb.2021.131330>
20. Juste-Dolz A, Fernández E, Puchades R et al (2023) Patterned biolayers of protein antigens for label-free biosensing in cow milk allergy. *Biosensors* 13:214. <https://doi.org/10.3390/bios13020214>
21. Loget G, Corn RM (2014) Silica nanowire arrays for diffraction-based bioaffinity sensing. *Chem Eur J* 20:10802–10810. <https://doi.org/10.1002/chem.201304800>
22. Avella-Oliver M, Ferrando V, Monsoriu JA et al (2018) A label-free diffraction-based sensing displacement immunosensor to quantify low molecular weight organic compounds. *Anal Chim Acta* 1033:173–179. <https://doi.org/10.1016/j.aca.2018.05.060>
23. Gatterdam V, Frutiger A, Stengele K-P et al (2017) Focal molography is a new method for the in situ analysis of molecular interactions in biological samples. *Nat Nanotechnol* 12:1089–1095. <https://doi.org/10.1038/nnano.2017.168>
24. Blickenstorfer Y, Borghi L, Reichmuth AM et al (2021) Total internal reflection focal molography (TIR-M). *Sensors Actuators B Chem* 349:130746. <https://doi.org/10.1016/j.snb.2021.130746>
25. Juste-Dolz A, Delgado-Pinar M, Avella-Oliver M et al (2021) BIO bragg gratings on microfibers for label-free biosensing. *Biosens Bioelectron* 176:112916. <https://doi.org/10.1016/j.bios.2020.112916>
26. Sypabekova M, Korganbayev S, González-Vila Á et al (2019) Functionalized etched tilted fiber Bragg grating aptasensor for label-free protein detection. *Biosens Bioelectron* 146:111765. <https://doi.org/10.1016/j.bios.2019.111765>
27. Chiavaioli F, Baldini F, Tombelli S et al (2017) Biosensing with optical fiber gratings. *Nanophotonics* 6:663–679. <https://doi.org/10.1515/nanoph-2016-0178>
28. Soares MS, Vidal M, Santos NF et al (2021) Immunosensing based on optical fiber technology: recent advances. *Biosensors* 11:305. <https://doi.org/10.3390/bios11090305>
29. Frutiger A, Tanno A, Hwu S et al (2021) Nonspecific Binding—fundamental concepts and consequences for biosensing applications. *Chem Rev* 121:8095–8160. <https://doi.org/10.1021/acs.chemrev.1c00044>
30. Juste-Dolz A, Delgado-Pinar M, Avella-Oliver M et al (2022) Denaturing for nanoarchitectonics: local and periodic UV-laser photodeactivation of protein biolayers to create functional patterns for biosensing. *ACS Appl Mater Interfaces* 14:41640–41648. <https://doi.org/10.1021/acscami.2c12808>
31. Rumpf RC, Garcia CR, Berry EA, Barton JH (2014) Finite-difference frequency-domain algorithm for modeling electromagnetic scattering from general anisotropic objects. *Prog Electromagn Res B* 61:55–67. <https://doi.org/10.2528/PIERB14071606>
32. Zhu Z, Brown T (2002) Full-vectorial finite-difference analysis of microstructured optical fibers. *Opt Express* 10:853. <https://doi.org/10.1364/OE.10.000853>
33. Freeman NJ, Peel LL, Swann MJ et al (2004) Real time, high resolution studies of protein adsorption and structure at the solid-liquid interface using dual polarization interferometry. *J Phys Condens Matter* 16:0–4. <https://doi.org/10.1088/0953-8984/16/26/023>
34. Micó G, Gargallo B, Pastor D, Muñoz P (2019) Integrated optic sensing spectrometer: concept and design. *Sensors* 19:1018. <https://doi.org/10.3390/s19051018>
35. Bru LA, Pastor D, Muñoz P (2021) Advanced and versatile interferometric technique for the characterization of photonic integrated devices. *Opt Express* 29:36503. <https://doi.org/10.1364/OE.435683>
36. Ding Z, Wang C, Liu K et al (2018) Distributed optical fiber sensors based on optical frequency domain reflectometry: a review. *Sensors* 18:1072. <https://doi.org/10.3390/s18041072>
37. Hua P, Ding Z, Liu K et al (2023) Distributed optical fiber biosensor based on optical frequency domain reflectometry. *Biosens Bioelectron* 228:115184. <https://doi.org/10.1016/j.bios.2023.115184>
38. Vörös J (2004) The density and refractive index of adsorbing protein layers. *Biophys J* 87:553–561. <https://doi.org/10.1529/biophysj.103.030072>
39. Bernard A, Renault JP, Michel B et al (2000) Microcontact printing of proteins. *Adv Mater* 12:1067–1070. [https://doi.org/10.1002/1521-4095\(200007\)12:14%3c1067::AID-ADMA1067%3e3.0.CO;2-M](https://doi.org/10.1002/1521-4095(200007)12:14%3c1067::AID-ADMA1067%3e3.0.CO;2-M)
40. Juste-Dolz A, Avella-Oliver M, Puchades R, Maquieira A (2018) Indirect microcontact printing to create functional patterns of physisorbed antibodies. *Sensors (Switzerland)* 18. <https://doi.org/10.3390/s18093163>

41. Wang J, Sanchez MM, Yin Y et al (2020) Silicon-based integrated label-free optofluidic biosensors: latest advances and roadmap. *Adv Mater Technol* 5:1901138. <https://doi.org/10.1002/admt.201901138>
42. Delamarche E, Pereiro I, Kashyap A, Kaigala GV (2021) Biopatterning: the art of patterning biomolecules on surfaces. *Langmuir* 37:9637–9651. <https://doi.org/10.1021/acs.langmuir.1c00867>

Publisher's note Springer Nature remains neutral with regard to jurisdictional claims in published maps and institutional affiliations.

Springer Nature or its licensor (e.g. a society or other partner) holds exclusive rights to this article under a publishing agreement with the author(s) or other rightsholder(s); author self-archiving of the accepted manuscript version of this article is solely governed by the terms of such publishing agreement and applicable law.